RESEARCH ARTICLE
PLANETARY SCIENCES

Earth and Planetary Physics
8: 711–727, 2024
doi: 10.26464/epp2024040

Magnetized magma intrusions being sources of a weak and a strong lunar magnetic anomaly revealed by 3D distribution of magnetization

HongYi Wang[1,2], Shuo Yao[1,2*], ZeLin Li[3], LiangHui Guo[1,2], Jing Yang[1], ChangLi Yao[1], Yuan Fang[1], and ZhaoJin Rong[4]

[1]School of Geophysics and Information Technology, Research Center of Lunar and Planetary Remote Sensing Exploration, China University of Geosciences (Beijing), Beijing 100083, China;

[2]Key Laboratory of Intraplate Volcanoes and Earthquakes (China University of Geosciences, Beijing), Ministry of Education, Beijing 100083, China;

[3]Hebei University of Engineering, Handan Hebei 056038, China;

[4]Key Laboratory of Earth and Planetary Physics, Institute of Geology and Geophysics, Chinese Academy of Sciences, Beijing 100029, China

Key Points:

- Three-dimensional distributions of magnetization under a strong and a weak lunar magnetic anomaly are recovered by magnetic inversion software.
- The depth range and volume of magnetic carriers support magnetized intruded magma as being the source of both magnetic anomalies.
- The recovered magnetization under Reiner Gamma supports the intensity of the dynamo field as being several microteslas 3.3 billion years ago.

Citation: Wang, H. Y., Yao, S., Li, Z. L., Guo, L. H., Yang, J., Yao, C. L., Fang, Y., and Rong, Z. J. (2024). Magnetized magma intrusions being sources of a weak and a strong lunar magnetic anomaly revealed by 3D distribution of magnetization. *Earth Planet. Phys.*, *8*(5), 711–727. http://doi.org/10.26464/epp2024040

Abstract: In this work, we aim to investigate the origin of the magnetic carriers in the lunar crust and the intensity of the ancient dynamo field. The magnetization and depth range of magnetic carriers are studied under a weak and a strong magnetic anomaly in Mare Tranquillitatis and in Oceanus Procellarum, respectively, where the surface ages are 3.6 and 3.3 billion years. A sophisticated three-dimensional amplitude inversion software program from a geophysical survey is used to reconstruct the distributions of magnetization in the lunar crust. Because no globally measured surface magnetic field exists for the Moon, a crustal magnetic anomaly model with a grid resolution of 0.2° is used. The depth range of the magnetic source is fixed by the boundary identified by a relative criterion, which is 20% of the recovered maximum magnetization. The central burial depths of the magnetic carriers are approximately 15 km and 25 km under Reiner Gamma and Mare Tranquillitatis, respectively. The volumes of the two magnetic sources are at scales of 10^4 and 10^5 km^3, respectively. The aforementioned differences may imply a hotter crust under Reiner Gamma than Mare Tranquillitatis by 3.3 billion years. The results support the view that the magma intrusions magnetized by an ancient magnetic field could be the origin of magnetic anomalies under Reiner Gamma and Mare Tranquillitatis. Compared with previous works, the maximum magnetization of 3 A/m under Reiner Gamma supports the intensity of the field being several microteslas.

Keywords: lunar magnetic anomaly; 3D distribution of magnetization; Reiner Gamma; Mare Tranquillitatis

1. Introduction

The lunar magnetic field was first measured by Apollo 12, 14, 15, and 16 at the landing sites on the lunar surface (Sonett and Mihalov, 1972; Dyal et al., 1974). The magnetic field is believed to be generated by remanent magnetization, and it varies from 3 to 300 nT at these sites. In addition, the lunar magnetic field has been measured in orbit by the Explorer satellite, the Apollo mission subsatellites, and later by the Lunar Prospector and Kaguya spacecraft. The first global maps of the crust magnetic anomalies in three components at 30 km altitude were provided by the Lunar Prospector (Richmond and Hood, 2008; Purucker and Nicholas, 2010). According to the higher altitude of Kaguya, a global map of the magnetic anomaly at an altitude of 100 km was obtained, which showed consistency with that from the Lunar Prospector (Baek et al., 2019). The magnetic anomalies are distributed widely at highlands, basins, and lunar maria (Wieczorek, 2018). No regular rules have been found between the anomalies and the geological structures (Oliveira and Wieczorek,

First author: H. Y. Wang, 3010220016@email.cugb.edu.cn
Correspondence to: S. Yao, yaoshuo@cugb.edu.cn
Received 19 FEB 2024; Accepted 02 APR 2024.
First Published online 01 AUG 2024.

2017). Usually, the directions of magnetization are different for different magnetic anomalies.

The origin of lunar magnetism has been studied by using measurements obtained in orbit or with crustal magnetic anomaly models (Hood and Spudis, 2016; Oliveira and Wieczorek, 2017; Baek et al., 2017). So far, two types of hypotheses have been discussed for the acquisition of lunar remanent magnetization. Some evidence supports the view that magnetic carriers are magmatic intrusions containing iron grains. They acquired the thermal remanent magnetization during slow cooling in a steady lunar dynamo field. Other evidence supports the perspective that magnetic sources are melted sheets or ejecta deposits caused by impacts (Hood and Spudis, 2016; Wieczorek, 2018; Hood et al., 2021). For example, the Imbrium impact is believed to have produced radial fractures that generated magmatic intrusions (Cai YZ et al., 2020), which are the anomaly sources (Hood et al., 2021). The impact-related hypothesis could explain the origins of both weak and strong anomalies. The main problem for the hypothesis of igneous sources is the low content of metallic iron (Fuller and Cisowski, 1990; Rochette et al., 2010). Lunar volcanic basalt samples are typically reported to contain only 0.08 wt.% of metallic iron (Hemingway and Tikoo, 2018).

The key evidence used to determine the origin of a magnetic anomaly includes the depths to the top and to the bottom of the magnetic source. The average depth of the magnetic carriers could be estimated by assuming the magnetic sources as dipoles or disks and calculating the Curie surface at the mantle–crust boundary, (Hood, 2011; Baek et al., 2017, 2019; Wieczorek, 2018). Different methods and orbital data have obtained significantly different central depths for the same anomaly, such as the northern anomaly in Mare Crisium (Hood, 2011; Takahashi et al., 2014; Baek et al., 2017). According to the results of a power spectrum analysis, Wieczorek (2018) reported that the depth to the top of the magnetic carriers from the surface was from 0 to 25 km. This means that both the magma intrusion and the impact may contribute to the lunar crust magnetic anomaly. However, it is impossible to constrain the depth to the bottom of the magnetized region or the Curie depth, as in previous works (Hemingway and Garrick-Bethell, 2012; Baek et al., 2017; Wieczorek, 2018).

Strong magnetic anomalies have been studied frequently, such as the famous Reiner Gamma swirl in Oceanus Procellarum (Kurata et al., 2005; Hemingway and Garrick-Bethell, 2012; Hemingway and Tikoo, 2018) and the northern anomalies in Mare Crisium (Baek et al., 2019, 2017). Assuming the magnetic sources to be a layer of dipoles, the calculated burial depth of the source under Reiner Gamma has been estimated as 8 to 15 km, the calculated direction of magnetization as an inclination between −6° and 5° and a declination between −18° and −3°, and with a magnetization intensity of greater than 0.5 A/m (Kurata et al., 2005; Hemingway and Garrick-Bethell, 2012; Oliveira and Wieczorek, 2017). The possible origins of swirls were analyzed by Hemingway and Tikoo (2018). The magnetization of mare basalt flows, impact melt sheets, or rocks that experienced cometary collisions is unlikely to have produced the narrow, elongate magnetic source bodies of the Reiner Gamma swirl. The impact ejecta deposits enriched in metals are presumed to be good candidates for generating the strong magnetization for the sources underlying the swirls. Dikes and lava tubes can best account for the narrow and often sinuous morphology. However, the sources of the strong anomalies in Mare Crisium are believed to be buried at depths between 20 and 40 km, as no swirl is shown on the surface (Baek et al., 2017). These strong anomalies under Mare Crisium are supposed to have a magnetized magma intrusion as the source.

In contrast to the strong anomaly, the weak fields have rarely been studied, and their origin is even more controversial (Hood and Spudis, 2016; Wieczorek, 2018). Because the intensities of magnetic anomalies vary significantly, there is an incorrect impression that only a small portion of the lunar crust was magnetized. In fact, the weak crustal magnetic fields are widely distributed when the intensity is shown in logarithmic scale. It has been suggested that these weak anomalies may have experienced demagnetization caused by an impact event or that they may not have been highly magnetized, either because of the higher temperature or because the materials underground contain smaller amounts of metallic iron grains (Wieczorek, 2018).

Above all, the sources for both strong and weak lunar crustal anomalies are unclear. To check the possible origins, it is necessary to carry out a comparative study between a weak anomaly and a strong anomaly. Though previous works have studied the source by layers of dipoles, the depth range and volume of the three-dimensional (3D) magnetic carriers as key types of evidence have not yet been determined.

In this work, a magnetic amplitude inversion is used to reconstruct the 3D distribution of magnetization underground. Such an amplitude inversion is not affected by the depth constraint of the source region and is not strongly affected by the uncertainty of the direction of magnetization. It is suitable for the condition of the Moon that the Curie depth and the direction of the ancient dynamo field are unclear. Taking a relative criterion, we identify the boundary of the magnetic carriers. Thus, the depth to the top, the depth to the bottom, and the volume of the magnetic carriers can be reasonably obtained. Among isolated anomalies, we select a weak anomaly, which is rarely studied, in Mare Tranquillitatis and the famous strong anomaly Reiner Gamma in Oceanus Procellarum for this comparative study. The two regions are chosen because they both have surface ages deduced by crater size-frequency distribution (Hiesinger et al., 2000; Chang YR et al. 2021) and their ages are on either side of 3.56 billion years, when the intensity of the ancient magnetic field dropped. The inversion method is introduced in Section 2. The key functions, the detailed solution, and synthetic tests of the inversion software used are provided in the Appendix. The inverted 3D distributions of magnetization for the two regions studied are shown and compared in Section 3. The possible origins of the magnetic sources are discussed in Section 4. The conclusions are drawn in Section 5.

2. Methods

This work uses a magnetic inversion software program for the unified direction of magnetization in the Cartesian coordinate system, which was originally proposed and developed at the University of British Columbia's Geophysical Inversion Facility

(UBC-GIF; Oldenburg and Li YG, 1994; Li YG and Oldenburg, 1996, 2003; Li YG et al., 2010). Detailed information on the software, including its validity and robustness, are provided at https://gif.eos.ubc.ca/software and at https://giftoolscookbook.readthedocs.io/en/latest/index.html. The copyright of the software belongs to UBC-GIF. The software package MAG3D v6.0 can be acquired at no cost for academic research.

2.1 Basic Theory

In this work, we briefly review the basic theories and key steps of the software used to show how this inversion works, including (1) the relation between the magnetization of underground cubes and the surface magnetic anomaly, (2) assumptions and constraints of the inversion, and (3) the objective function of the inversion and its solution.

2.1.1 Relation between the magnetization of underground cubes and the surface magnetic anomaly

The underground space is divided equally into cuboid cells. The magnetization is uniform in one cuboid cell. The direction of magnetization of all the cells is assumed to be the same. This means that all the cells acquired magnetization under the same magnetic field, as shown in Figure 1. A right-handed Cartesian coordinate system is used, in which x directs to the north, y directs to the east, and z is downward. The magnetic anomaly vector at one site on the surface caused by one magnetized cuboid cell can be calculated by

$$\boldsymbol{B}_a = \boldsymbol{Tm}. \tag{1}$$

In Equation (1), $\boldsymbol{B}_a = (H_{ax}, H_{ay}, Z_a)$ represents the magnetic anomaly vector at one site, and $\boldsymbol{m} = (m_x, m_y, m_z)$ represents the magnetization vector. Element T_{ij} in matrix $\boldsymbol{T}$ can be calculated (Bhattacharyya, 1964; Rao and Babu, 1991) by

$$T_{ij} = \frac{\mu_0}{4\pi}\iiint \frac{\partial}{\partial S_i}\frac{\partial}{\partial S_j}\frac{1}{|r - r_0|}\mathrm{d}v. \tag{2}$$

In Equation (2), $i = 1, 2, 3$, and $j = 1, 2, 3$, whereas S_1, S_2, S_3 represent x, y, z in the Cartesian coordinate system.

According to Equation (2), the measured magnetic anomaly vectors at sites in a line can be calculated by the cuboid cells in a line underground:

$$\boldsymbol{d} = \boldsymbol{GM}. \tag{3}$$

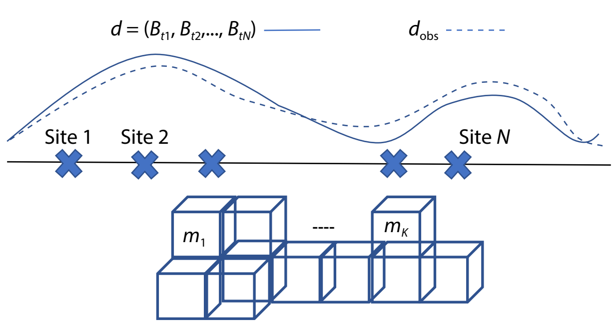

Figure 1. Scenario of 3D magnetic inversion in Cartesian coordinates. The underground space is divided equally into cuboid cells.

In Equation (3), $\boldsymbol{d} = (d_1, d_2, \ldots, d_N)$ is an array of magnetic anomaly vectors at N sites along a line, where N is the sequence number of points; d_i is $\boldsymbol{B}_a$ for each site (defined in Equation (1)); $\boldsymbol{M} = (m_1, m_2, \ldots, m_k)$ is an array that includes magnetization vectors in cuboid cells along a line underground; and K is the sequence number of the cuboid cells. The matrix $\boldsymbol{T}$ can be identified as representing the relation between one magnetized cube and the magnetic anomaly at one site on the surface. In Equation (3), matrix $\boldsymbol{G}$ represents the relation between a line of magnetized cubes and the magnetic anomalies at sites along a line on the surface. The matrix $\boldsymbol{G}$ has elements g_{ij} that quantify the contribution of a unit magnetization in the jth cell to the ith datum of the magnetic anomaly. For example, g_{11} represents the relation between the magnetization of cell 1 underground (m_1) and its contribution to the magnetic anomaly at site 1 (B_{a11}) on the surface. According to Equation (1), if $B_{a11} = \boldsymbol{T}m_1$, then $g_{11} = \boldsymbol{T}$, where $\boldsymbol{T}$ is defined by Equation (2). It should be noted that for different cells underground, the related $\boldsymbol{T}$ is different because the position vectors of the cells are different. In Cartesian coordinates, Equation (3) could be expressed for each direction:

$$\begin{aligned} \boldsymbol{H}_{ax} &= \boldsymbol{G}_x\boldsymbol{m}, \\ \boldsymbol{H}_{ay} &= \boldsymbol{G}_y\boldsymbol{m}, \\ \boldsymbol{Z}_a &= \boldsymbol{G}_z\boldsymbol{m}. \end{aligned} \tag{4}$$

2.1.2 Objective function of inversion

The objective function of inversion contains two parts: the model difference and the data misfit. Once the weighted sum of the two parts approaches the minimum, the optimized result is selected, as shown in Equation (A1). That is because when the distribution of magnetization varies, the difference between the current distribution and the initial model increases, but the misfit between the measured magnetic anomaly ($\boldsymbol{d}_{\mathrm{obs}}$) and the recovered one ($\boldsymbol{d}$) decreases. The model objective function of underground magnetization and the process of solving the final optimized magnetization distribution are provided in the Appendix. Because the Curie depth and direction of magnetization are unclear, and the grid resolution of the lunar surface magnetic anomaly model is much larger than that on the Earth, we check the validity of this amplitude inversion, which is also shown in Figures A1–A3.

2.1.3 Assumptions and constraints of the inversion

Two assumptions are made in the inversion. One is the direction of magnetization. The other is the field decay along the depth. The decay along the depth is taken as part of the model objective function, which is related to the shape of the magnetized materials. In this work, we assume the magnetized body to be sphere shaped. The details of the depth weighting function are provided in the first section of the Appendix.

In the inversion used, all the cube cells are assumed to have the same direction of magnetization. The direction is also assumed. The result of the inversion is the magnitude of magnetization of each cube cell. Considering the physical properties, the magnitude of magnetization m is always larger than 0. The initial model of magnetization underground m_0 is set as 10^{-4} A/m, which is the default used in the software. It should be mentioned that m_0 could be any small value larger than 0 and smaller than 1. Different values of m_0 will affect the time to achieve convergence during inversion and will affect the final distribution of magnetization little.

In the inversion software, the data can be either the component or the total magnitude of the magnetic anomaly. In this work, we take the total amplitude of the magnetic anomaly (B_t) as the input data because it is not sensitive to the direction:

$$B_t = \sqrt{H_{ax}^2 + H_{ay}^2 + Z_a^2}. \tag{5}$$

Because the amplitude of the magnetic anomaly does not contain information on the direction, the amplitude inversion is affected less by the uncertainty of the direction of magnetization than are the inversions of other components (Nabighian, 1972). When the direction of magnetization is very complex, the amplitude inversion shows better results than the component inversion under the same assumed direction (Li YG et al., 2010). Although the amplitude inversion is less affected by direction, errors still appear in the burial depth and volumes. The uncertainty caused by direction is checked in Figure A3. In our study, the directions of the remanent magnetization calculated from the surface magnetic anomaly vectors are very complex in the two lunar maria, as shown in Figure A4. Therefore, we choose the amplitude inversion mode of the inversion software. Another problem is how to assume a unified magnetization direction for inversion in the two lunar maria studied. The direction is composed of inclination and declination. To avoid errors from declination in the inversion itself, we choose the vertical magnetization assumption. In that case, the declination does not make sense. The inversion results related to different declinations are the same. Such a feature could be used to double check the inversion results, so we simply assume the inclination to be −90°.

Finally, we would like to mention that there is a curvature effect when using the Cartesian framework because the two regions of magnetic anomalies studied cover a spatial distance of less than 10° along the longitude and latitude. According to Lane (2009), the error would be approximately 1%.

3. Results

3.1 Weakly Magnetized Materials under Mare Tranquillitatis

We use the surface magnetic field model established by Tsunakawa et al. (2014, 2015) to study the possible source of magnetization under a weak magnetic anomaly in Mare Tranquillitatis and a strong anomaly in Oceanus Procellarum. Oliveira and Wieczorek (2017) also used such a model to study the underground magnetization. The surface ages of the two regions studied are similar, in that the weak one is 3.6 billion years old and the strong one is 3.3 billion years old (Hiesinger et al., 2000, 2003). Because the inclinations of the magnetic anomalies at the two regions studied are very complex, as shown in Figure A4, it is difficult to determine the unique direction of magnetization. Therefore, amplitude inversion is a suitable tool that is weakly affected by the uncertainty of the direction of magnetization (Nabighian, 1972), as shown in Figure A3. In this study, the direction of magnetization is assumed to be inclination (I) = −90° and declination (D) = 0°.

In Mare Tranquillitatis, we use the grid data of the crustal magnetic field model from 36°E to 40.8°E and from 7.4°N to 10.6°N. The three components and amplitude of the magnetic anomalies on the surface of the studied area in Mare Tranquillitatis are shown in Figure 2. The maximum amplitude of the magnetic anomaly in this area is approximately 21 nT. The position of the maximum magnetic anomaly is 39.3°E, 9.1°N. The grid resolution of the surface magnetic anomaly model is 0.2°, which equals approximately 6 km.

We also check the elevation and image in the studied area, as shown in Figures 2e and 2f. Figure 2e is from an improved lunar digital elevation model presented by Barker et al. (2016). The highest elevation of this area is approximately 100 m, and the lowest elevation is approximately −2700 m. The ground level of almost the entire area is below 0 m. A high-resolution image of this area taken by Lunar Reconnaissance Orbiter Camera (LROC) Narrow Angle Cameras (NACs) is from https://quickmap.lroc.asu.edu/ and is overlaid on the Wide Angle Camera (WAC) Global Morphologic base map, as shown in Figure 2f. The contours of the lowest areas can be identified clearly as being located in the middle and the northeast corner of the area, respectively. The boundaries of these areas are obviously higher than the surrounding areas. However, these regions have little relevance to the main magnetic anomaly.

Because the Curie depth on the Moon is unclear and the depths of magnetic carriers are suggested as being from 40 to 90 km under Mare Crisium, with a surface age from 3.6 to 3.9 billion years (Baek et al., 2019), we check the reliability of our inversion with different depth constraints of the inversion region. The bottom depths of the inversion region are set as 30, 60, 90, and 120 km. The 3D distributions of magnetization under Mare Tranquillitatis recovered by amplitude inversion are shown in Figure 3. The grid spacing in the inversion region underground is set as 0.1°, which is approximately 3 km. It is interesting that the magnetization is not convergent and shows a maximum at the bottom of the inversion region when the depth constraint of the inversion region equals 30 km. Compared with the test results for the ball model shown in Figure A1 in the Appendix, this means the bottom of the magnetized body under Mare Tranquillitatis is deeper than 30 km. When the bottom depth of the inversion region increases to 60 km, the distribution of magnetization becomes convergent. The boundaries of the magnetized bodies defined by 20% of the maximum magnetization show similar depth ranges for the bottom depths of the inversion region being 90 and 120 km. To check the solidity of the inversion results, we also show the forward-calculated surface anomalies according to the inversion results in the last row of Figure 3. The correlation coefficients between the forward-calculated surface anomaly and the lunar anomaly model used are 0.9931, 0.9948, 0.9958, and 0.9960 for the depth constraints of 30, 60, 90, and 120 km, respectively.

Next, the depths to the top and to the bottom of the magnetic carriers are identified by the contour of 20% of maximum magnetization, which is shown as the dashed white contours in Figure 3. This criterion is fixed from the model tests shown in Figures A1–A2. The depth ranges and volumes of the magnetic carriers recovered by inversion under Mare Tranquillitatis are listed in

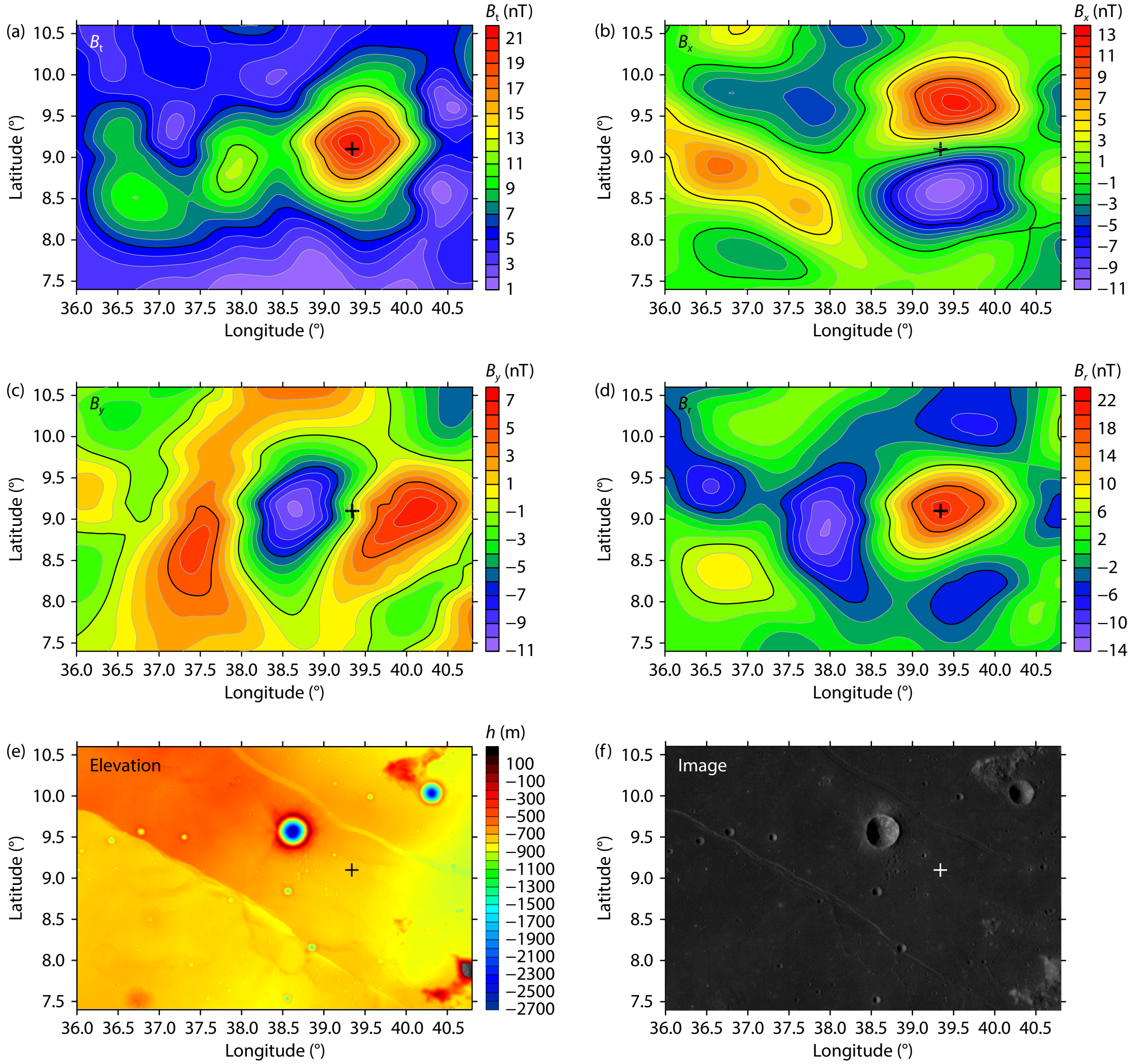

Figure 2. Distributions of magnetic anomaly vectors, elevation, and high resolution image in Mare Tranquillitatis. The total magnitude, north component, east component, and radial component of the magnetic anomalies studied are shown in panels (a) to (d). The elevation and image are shown in panels (e) and (f). The plus signs mark the maximum amplitude of the magnetic anomaly.

Table 1. The maximum remanent magnetization in red is 0.08 A/m. The depth to the top of the magnetic carriers is 3.00 km in latitude–depth profile and longitude–depth profile. The maximum magnetization corresponding to the center of the magnetic carrier is approximately 24 km. The horizontal slices related to the center of magnetic carriers are shown in the third row of Figure 3. The depth to the bottom identified by the 20% maximum magnetization is 54 km in latitude–depth profile and 50 km in longitude–depth profile when the depth constraint equals 90 km. The volume of the magnetic carriers is approximately 170,000 km^3.

3.2 Strongly Magnetized Materials under Oceanus Procellarum

An area showing a strong magnetic anomaly in Oceanus Procellarum is studied, which is called Reiner Gamma (Hemingway and Garrick-Bethell, 2012; Hemingway and Tikoo, 2018). The magnetic anomaly is well known to be accompanied by a swirl. The region for inversion is from 299° to 304° in longitude and from 6° to 9° in latitude. Three components and the total intensity of the lunar magnetic anomalies in this region are shown in Figure 4. The elevation and high resolution image from LROC NACs are shown in Figures 4e and 4f. The maximum amplitude of the magnetic anomaly in the region studied is approximately 500 nT, which exceeds that of most of the lunar surface. The position of the maximum magnitude of the magnetic anomaly is 302°E, 7.4°N. The magnetic intensity seems to have little relevance to the elevation of this region.

The reconstructed 3D distributions of magnetization with different bottom depths of inversion regions are shown in the top three

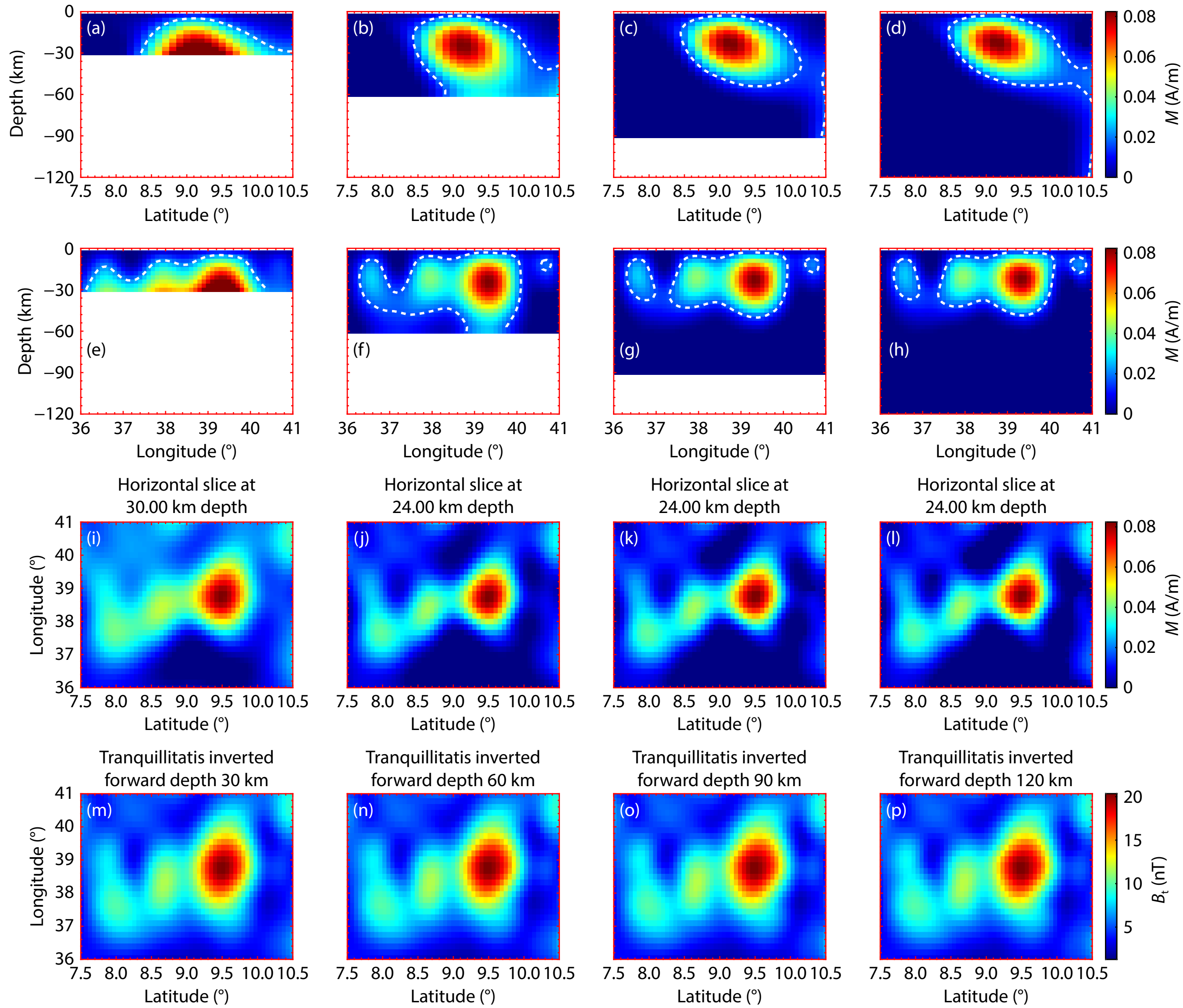

Figure 3. Three-dimensional distributions of magnetization recovered by amplitude inversion with different depth constraints under Mare Tranquillitatis. From left to right, the bottom depth of the underground inversion region is set to be 30, 60, 90, and 120 km. The top row shows the results in depth–latitude profiles at 39.3°E. The second row shows the distributions of magnetization in depth–longitude profiles at 9.1°N. The horizontal slices at the depth related to maximum magnetization are shown in the third row. The forward-calculated surface anomalies (B_t) are shown in the bottom row. The dashed white contours denote the magnetization as 20% of the maximum.

Table 1. Depth ranges and volumes of the magnetized body under Mare Tranquillitatis recovered by inversion.

Depth constraint (km)	Profile	Top (km)	Max (km)	Bottom (km)	Volume (km^3)
30	Latitude	−4.89	−30	−30	99,650.0
	Longitude	−4.9	−30	−30	
60	Latitude	−3.02	−24	−60	206,621.9
	Longitude	−3.01	−24	−60	
90	Latitude	−3	−24	−54.14	168,572.3
	Longitude	−3	−24	−50.17	
120	Latitude	−3	−24	−53.59	176,487.7
	Longitude	−3	−21	−48.71	

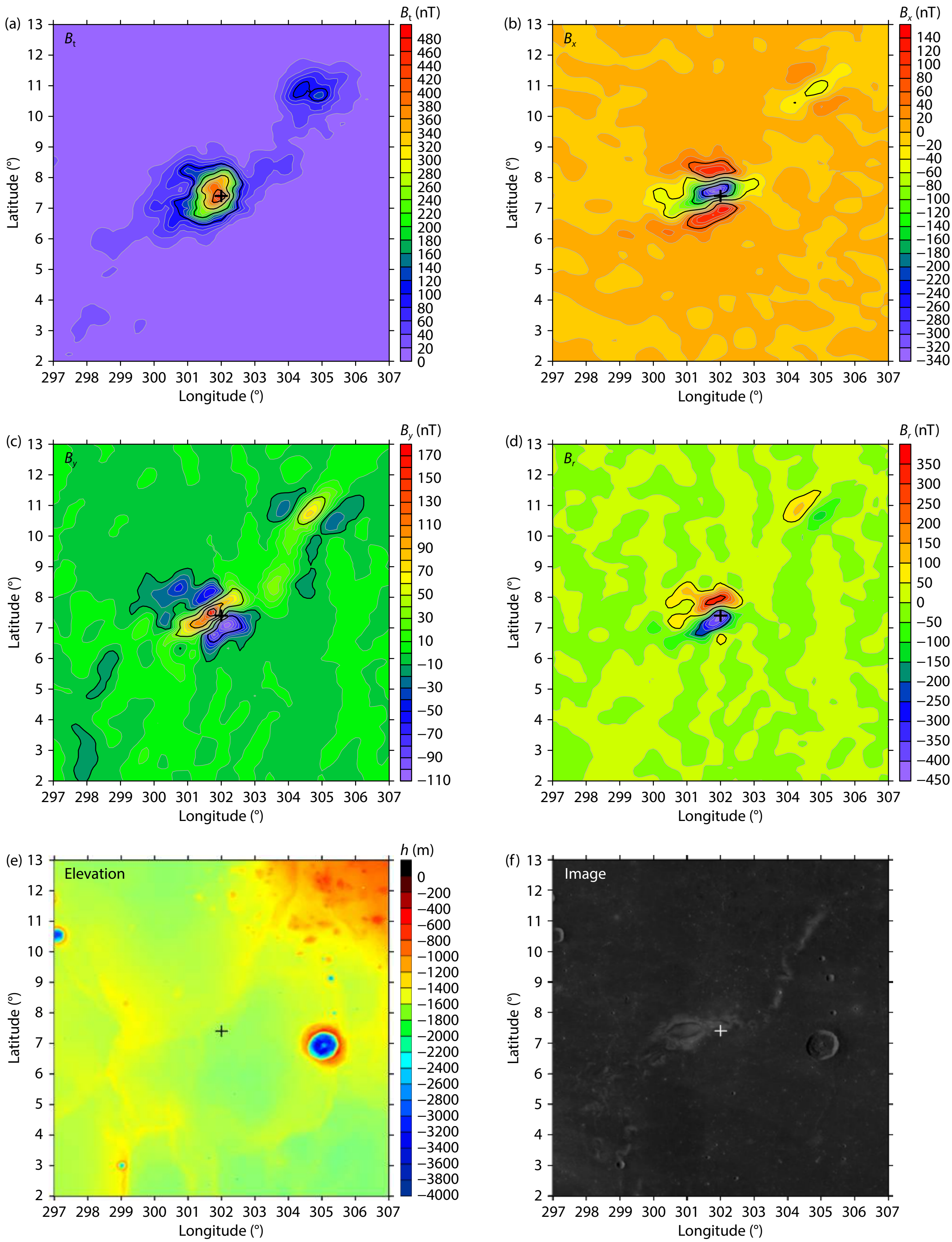

Figure 4. Distributions of the magnetic anomaly, elevation, and high resolution image in Oceanus Procellarum. The total magnitude, north component, east component, and radial component of the surface magnetic anomalies studied are shown in panels (a) to (d). The elevation and image are shown in panels (e) and (f). The plus signs mark the maximum of the magnetic anomaly.

rows of Figure 5. We can identify that the maximum remanent magnetization under Reiner Gamma is approximately 3.0 A/m. Obviously, the maximum remanent magnetization here is more than 15 times stronger than that in Mare Tranquillitatis. The depth to the bottom and the depth to the top of the magnetic source under Reiner Gamma in Oceanus Procellarum can be estimated by the distribution of magnetization. The depths to the top and to the bottom of the magnetic carriers as related to different depth constraints of the inversion region are shown in Table 2.

The depth to the bottom of the magnetic carriers is approximately 30 km. The center of the magnetic carrier defined by the maximum magnetization is at a depth of approximately 15 km. The horizontal slices of magnetization related to the center of the magnetic carriers are shown in the third row of Figure 5. The depth to the top is 1.5 km. It is interesting that although the magnitude of the magnetic anomaly at Reiner Gamma is much stronger than that at Mare Tranquillitatis, the depths to the top of the magnetic carriers are quite similar. For the depth to the bottom, Reiner Gamma shows a different, shallower source than that under Mare Tranquillitatis. We should clarify that the upper limit of the inversion region underground is 1.5 km. This is caused by the grid spacing of inversion being 0.1° (3 km), which is half that in the lunar magnetic anomaly model used. This means that the real top of the magnetic carriers may be even closer to the surface.

The volume of the magnetic carriers under Reiner Gamma is approximately 25,000 km^3. Note that the volumes of the magne-

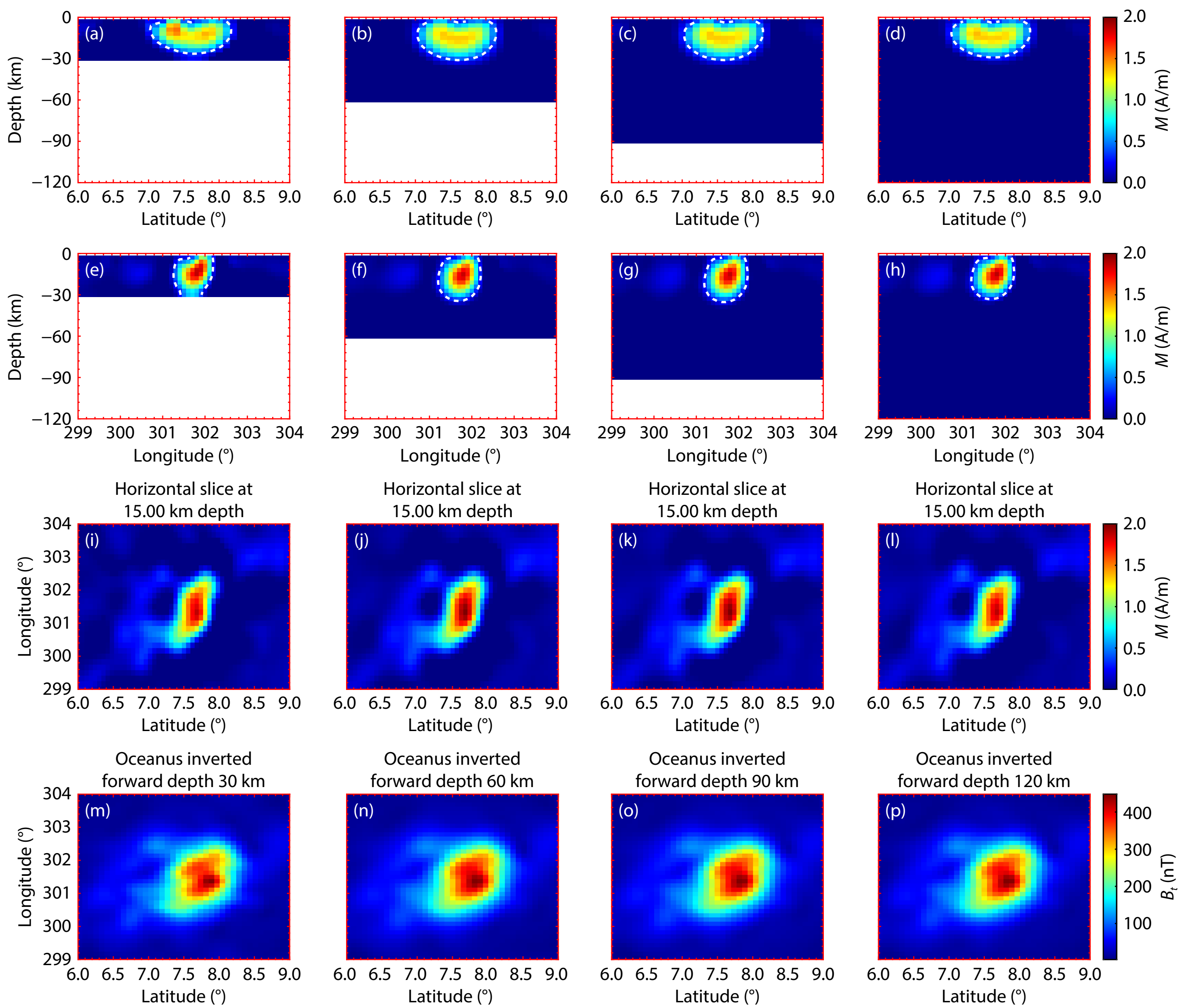

Figure 5. Three-dimensional distributions of magnetization under Reiner Gamma recovered by amplitude inversion. In the first row, from left to right, the four panels show the distribution of magnetization in the profiles of depth versus latitude at 302°E related to depth constraints of the inversion region at 30, 60, 90, and 120 km. In the second row, the distribution of magnetization in profiles of depth versus longitude at 7.4°N are shown. The horizontal slices of magnetization at the depth related to maximum magnetization are shown in the third row. The bottom row shows the forward-calculated surface anomalies related to the four depth constraints. The dashed white contours denote 20% of the maximum magnetization.

Table 2. Depth ranges and volumes of the magnetized body under Reiner Gamma recovered by inversion.

Depth constraint (km)	Profile	Top (km)	Max (km)	Bottom (km)	Volume (km^3)
30	Latitude	−1.5	−9	−26.49	23,648.91
	Longitude	−1.5	−15	−30	
60	Latitude	−1.5	−15	−31.13	25,622.96
	Longitude	−1.5	−15	−34.52	
90	Latitude	−1.5	−15	−31.1	26,241.49
	Longitude	−1.5	−15	−35.3	
120	Latitude	−1.5	−12	−29.14	24,368.01
	Longitude	−1.5	−15	−33.1	

tized materials under the two maria are at different scales. The volume of the magnetized body under Reiner Gamma is approximately 10^4 km^3 and that under Mare Tranquillitatis is at a scale of 10^5 km^3. Considering that the grid resolution of the crustal anomaly model is 6 km and that the grid spacing of the inversion is 3 km, the real magnetic carriers may not be in only one bulk. To check the solidity of the inversion results, the forward-calculated surface anomalies according to the inversion results are shown in the last row of Figure 5. The correlation coefficients between the forward-calculated surface anomalies and the lunar anomaly model used are 0.9966, 0.9952, 0.9968, and 0.9970 for the depth constraints of 30, 60, 90, and 120 km, respectively.

4. Discussion

4.1 Depth Range and Curie Surface

It is possible that the depth to the bottom of the magnetic carriers is close to the Curie surface. The Curie surface is an interface where the rocks below it will not obtain remanent magnetization and where the ferromagnetism transfers to paramagnetism. If the carriers of remanent magnetization are metallic iron grains, which are the dominant ferromagnetic materials on the Moon, the Curie temperature is approximately 1040 K. Iron sulfides also play a minor role under certain circumstances. This material has a lower Curie temperature, at 600 K. According to the temperature profiles reported by Miljković et al. (2015), the maximum depths to the Curie temperature of metallic iron are between 30 and 120 km. Considering that the results of amplitude inversions can recover rather accurate depths of the magnetic sources, as shown in Table A1, the depths to the bottom of the magnetic carriers under Mare Tranquillitatis and Reiner Gamma are approximately 50 km and 30 km, respectively. The different depths to the bottom of the magnetic carriers suggest that the temperature in the lunar crust under the two maria may be different. The crust under Mare Tranquillitatis is probably cooler. Thus, for Mare Tranquillitatis, the weaker magnetization is probably not due to a higher temperature underground (Wieczorek, 2018).

Note that although the surface age of Oceanus Procellarum is 3.3 billion years, which is younger than that of Mare Tranquillitatis, it is possible that the magnetic carriers underground are older. Considering that the lunar ancient dynamo field dropped severely at 3.56 billion years (Tikoo et al., 2017) and that Reiner Gamma in Oceanus Procellarum shows much stronger magnetization in the crust, the magnetic carriers may have been formed before 3.6 billion years. It should also be mentioned that the depth to the bottom of the magnetic carriers could be slightly affected by an inaccurate magnetization direction, as shown in Figure A3 and Table A1.

4.2 Possible Source of the Magnetic Carriers

Our inversion results show that the horizontal scale of the magnetic carriers is approximately 30 km. The depth to the center of the magnetic carriers under Reiner Gamma is approximately 15 km and that to the bottom is approximately 30 km. The depth to the center and that to the bottom of the magnetized body under Mare Tranquillitatis are 25 km and 50 km, respectively. The aforementioned depth ranges suggest that a magnetized magma intrusion could be the origin of the anomalies studied. In addition, the magnetic sources under Mare Tranquillitatis and Reiner Gamma may have become magnetized in different lengths of time because the time required to obtain magnetization is related to the burial depth (Baek et al., 2019).

The depth to the top of the magnetic carriers is constrained by the grid spacing of inversion. Because the grid spacing underground is 0.1°, which equals 3 km, this means that the top of the source region underground is 1.5 km. It should be mentioned that the model reported by Tsunakawa et al. (2015) consisted of observations of the lunar magnetic field measured at 10- to 45-km altitudes by the Kaguya and Lunar Prospector spacecraft, but the model lacks anomalies measured at lower altitudes. This means that the real depth to the top of the magnetic carriers under Reiner Gamma could be even closer to the surface than those obtained in this work.

It should also be mentioned that Hemingway and Garrick-Bethell (2012) and Garrick-Bethell and Kelley (2019) have studied the magnetic source of Reiner Gamma. Garrick-Bethell and Kelley (2019) reported a magnetization of approximately 66 A/m for a 160-m-thick dipole layer, much larger than that in this work. In Garrick-Bethell and Kelley (2019), the magnetic source was assumed to be a magnetized melt sheet from an oblique impact. They used dipoles to represent the magnetic carriers. The dipole layer was assumed to be very thin, and the width was assumed to be 2 km. The depth of the dipoles was fixed by a least-squares best fit with varying depths from 0 to 20 km, taking 1 km as the step length. It should be noted that the thickness of ejecta is not easy to estimate (Cai YZ et al. 2020). Compared with their work, we do not hold any preference as to the origin of the magnetic carriers. The thickness and width of the magnetic carriers are much larger in our inversion results, so the calculated magnetization is one order smaller in our work. On the other hand, the burial depth of the dipoles and the central burial depth of the magnetic carriers reported in their work and in our work, respectively, are similar. Because the thickness and width of the magnetic source are much larger than the assumption in Hemingway and Garrick-Bethell (2012), and Garrick-Bethell and Kelley (2019), our work supports the view that a magnetized magma intrusion, and not only melt materials by impact, could also be the source of Reiner Gamma.

Finally, the volumes of the magnetic carriers obtained in our work are also consistent with what one might expect for a magmatic sill, so we tend to suggest that the magnetized material is related to magmatic intrusions (Wieczorek, 2018). The inverted 3D distribution of magnetization under Reiner Gamma on the surface of Oceanus Procellarum also supports the perspective that dikes and lava tubes are possible origins of the crustal magnetic anomalies (Hemingway and Tikoo, 2018).

The inverted densities from both Gravity Recovery and Interior Laboratory (GRAIL) measurements (Zuber et al., 2013) and from Apollo surface seismic measurements (Weber et al., 2011) suggest that the average thickness of the lunar crust is between 34 and 43 km and that the thickness of the lunar crust can be 80 km locally (Wieczorek et al., 2013). Thus, the bottom of the magnetic carriers obtained in this work are in the deep crust or the crust–mantle boundary.

Our inverted distribution of magnetization under Reiner Gamma matches the theory that a 30- to 50-km-deep mantle source is predicted to produce dikes and that the top of this magma intrusion could be within 1 km of the surface (Wilson and Head, 2017). It is possible that the strong and weak magnetization under the two regions studied were caused by different contents and sizes of metallic iron grains or by different crystal structures of the magmatic rocks.

Because the contents of magnetized metallic grains contribute to the density of rocks underground, we also check the gravity anomaly in both regions, as shown in Figure 6. The gravity anomaly is calculated from the model available at https://pds-geosciences.wustl.edu/grail/grail-l-lgrs-5-rdr-v1/grail_1001/shadr/. The spherical harmonic degree of this model is 1200, leading to a grid resolution of 4.5 km (Goossens et al., 2016). It is obvious that the weak field region shows a much smaller Bouguer gravity anomaly, whereas the strong field region shows a stronger Bouguer gravity anomaly. This means that the materials under the entire area of study in Mare Tranquillitatis are lighter than those under Reiner Gamma in Oceanus Procellarum. However, the area related to the magnetic anomaly does not show a stronger Bouguer gravity anomaly than each mare studied in its neighborhood. This means that the magnetic carriers do not have a significantly different density from their surrounding rocks. More information is needed to check the contents of the metallic iron grains in the magnetized rocks.

5. Conclusions

This study focuses on the origins of magnetic sources under lunar maria. The key pieces of evidence are the depth ranges and volumes obtained from 3D distributions of magnetization by inversion. Two regions showing significantly different strengths of crustal magnetic anomalies are studied. One shows a weak magnetic anomaly in Mare Tranquillitatis, and the other shows a strong magnetic anomaly with a swirl called Reiner Gamma in Oceanus Procellarum. This work applies 3D inversion of the

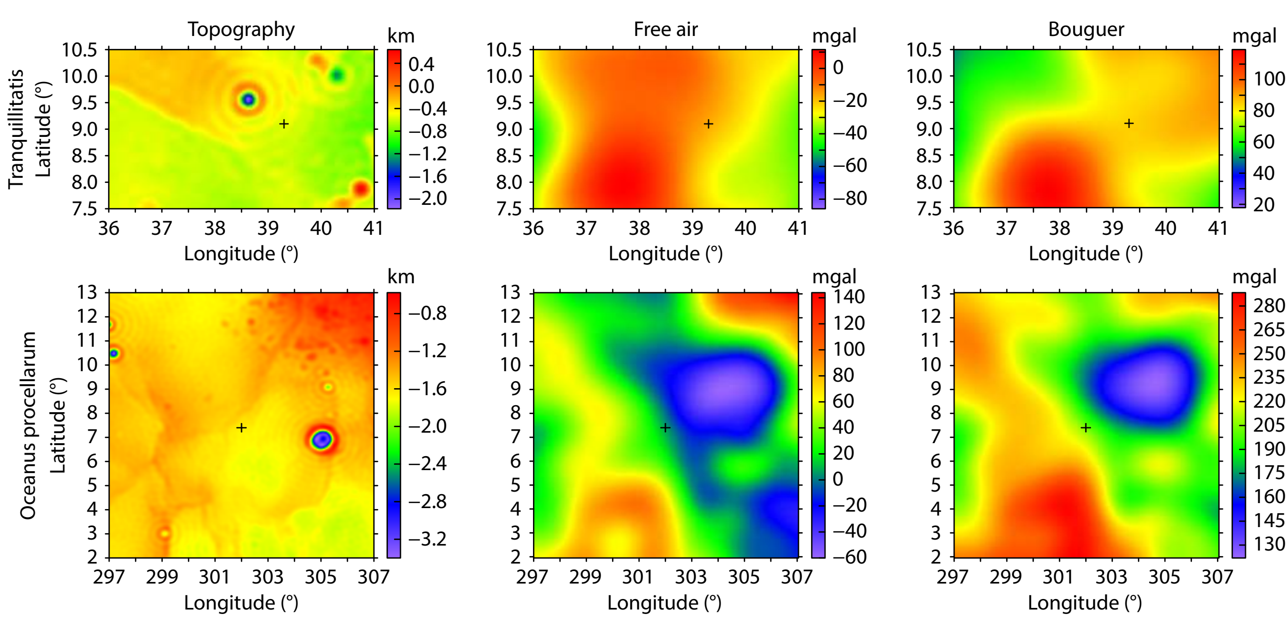

Figure 6. Topography, free air gravity anomaly, and Bouguer gravity anomaly in the two regions studied. From left to right, the panels show the topography, the free-air gravity anomaly, and the Bouguer gravity anomaly. The top row shows those for Mare Tranquillitatis, and the bottom row shows those for Oceanus Procellarum. The plus signs mark the maximum of the magnetic anomaly in each region.

magnetic anomaly amplitude without an assumption for the thickness and depth of the magnetic sources. For the first time, depth ranges and volumes of the magnetic carriers are obtained from the recovered 3D distribution of magnetization. The depth ranges of the magnetic carriers support the view that the sources of both the strong and weak anomalies could be a magma intrusion magnetized by an ancient lunar magnetic field.

The depth and volume of magnetic carriers under Mare Tranquillitatis align with the possibility that dikes intrude only into the crust, without erupting on the surface. For Reiner Gamma, the depth range and magnetization of the magnetic carriers support a possible magma eruption on the surface. This matches the explanation that dikes and lava tubes form the swirl (Hemingway and Tikoo, 2018).

Our results also contribute indirectly to the understanding of the ancient lunar magnetic field. Compared with the work of Garrick-Bethell and Kelley (2019), the magnetization obtained in the present work supports the intensity of the ancient dynamo field as being several microteslas. Because Garrick-Bethell and Kelley (2019) stated that their results are near the upper bounds for chondrites (Wieczorek et al., 2012) and the Moon's paleomagnetic field (Weiss and Tikoo, 2014), the magnetization and the related intensity of the ancient field obtained in our work are more sensible and align with the results reported by Weiss and Tikoo (2014).

Because the depth to the bottom of the magnetic source is related to the Curie temperature, the two regions studied possibly once had different temperatures in the lunar crust. It is possible that the crust under Mare Tranquillitatis was cooler than that under Oceanus Procellarum. It has been suggested that the intensity of the ancient dynamo field dropped to 10% approximately 3.56 billion years ago according to paleomagnetism studies on the returned samples (Weiss and Tikoo, 2014; Tikoo et al., 2017). However, the weak anomaly studied with an older surface age of 3.6 billion years showed a much weaker magnetization, and the strong anomaly with a younger surface age of 3.3 billion years showed 10 times stronger magnetization. Considering that a dynamo is closely related to the thermal states (Weiss and Tikoo, 2014; Jiang CZ and Yao S, 2019), it is possible that the underground materials in the two regions are both older than 3.6 billion years or that the ancient magnetic field did not drop so severely. Above all, the varied intensity of the dynamo field may not be the reason the anomalies studied in this work are weak and strong.

In this study, amplitude inversion with an assumed unified vertical direction of magnetization is used because amplitude inversion is less affected by an inaccurate direction. An important question for inversion is how to deal with the complex magnetization direction of lunar remanent magnetization. In the future, we will attempt to apply inversion for a magnetization vector on a lunar magnetic anomaly and check the adaptability and stability.

Acknowledgments

This work was supported by the National Key R&D Program of China (Grant No. 2021YFA0715101). S. Yao was supported by the Chinese 111 Project (Contract No. B20011) and by the Fundamental Research Funds for the Central Universities. H. Y. Wang was supported by the Innovation Experimental Class Program. The 3D magnetic inversion algorithm and the code were originally developed under the consortium research project Joint/Cooperative Inversion of Geophysical and Geological Data, University of British Columbia–Geophysical Inversion Facility (UBC-GIF), Department of Earth and Ocean Sciences, Vancouver, British Columbia. S. Yao thanks Z. Ma and T. Yang for their helpful discussions.

References

Baek, S. M., Kim, K. H., Garrick-Bethell, I., Jin, H., Lee, H. J., and Lee, J. K. (2017). Detailed study of the Mare Crisium northern magnetic anomaly. *J. Geophys. Res.: Planets*, *122*(2), 411–430. https://doi.org/10.1002/2016JE005138

Baek, S. M., Kim, K. H., Garrick-Bethell, I., and Jin, H. (2019). Magnetic anomalies within the Crisium Basin: magnetization directions, source depths, and ages. *J. Geophys. Res.: Planets*, *124*(2), 223–242. https://doi.org/10.1029/2018JE005678

Barker, M. K., Mazarico, E., Neumann, G. A., Zuber, M. T., Haruyama, J., and Smith, D. E. (2016). A new lunar digital elevation model from the lunar orbiter laser altimeter and SELENE terrain camera. *Icarus*, *273*, 346–355. https://doi.org/10.1016/j.icarus.2015.07.039

Bhaskara Rao, D., and Ramesh Babu, N. (1991). A rapid method for three-dimensional modeling of magnetic anomalies. *Geophysics*, *56*(11), 1729–1737. https://doi.org/10.1190/1.1442985

Bhattacharyya, B. K. (1964). Magnetic anomalies due to prism-shaped bodies with arbitrary polarization. *Geophysics*, *29*(4), 517–531. https://doi.org/10.1190/1.1439386

Cai, Y. Z., Xiao, Z. Y., Ding, C. Y., and Cui, J. (2020). Fine debris flows formed by the Orientale basin. *Earth Planet. Phys.*, *4*(3), 212–222. https://doi.org/10.26464/epp2020027

Cella, F., and Fedi, M. (2012). Inversion of potential field data using the structural index as weighting function rate decay. *Geophys. Prospect.*, *60*(2), 313–336. https://doi.org/10.1111/j.1365-2478.2011.00974.x

Chang, Y. R., Xiao, Z. Y., Wang, Y. C., Ding, C. Y., Cui, J. and Cai, Y. Z. (2021). An updated constraint on the local stratigraphy at the Chang'E-4 landing site. *Earth Planet. Phys.*, *5*(1), 19–31. https://doi.org/10.26464/epp2021007

Dyal, P., Parkin, C. W., and Daily, W. D. (1974). Magnetism and the interior of the moon. *Rev. Geophys.*, *12*(4), 568–591. https://doi.org/10.1029/RG012i004p00568

Farquharson, C. G., and Oldenburg, D. W. (2004). A comparison of automatic techniques for estimating the regularization parameter in non-linear inverse problems. *Geophys. J. Int.*, *156*(3), 411–425. https://doi.org/10.1111/j.1365-246X.2004.02190.x

Fuller, M., and Cisowski, S. M. (1990). Lunar paleomagnetism. In D. E. James (Ed.), *Encyclopedia of Solid Earth Geophysics* (pp. 668–673). New York: Springer. https://doi.org/10.1007/0-387-30752-4_83

Garrick-Bethell, I., and Kelley, M. R. (2019). Reiner Gamma: a magnetized elliptical disk on the Moon. *Geophys. Res. Lett.*, *46*(10), 5065–5074. https://doi.org/10.1029/2019GL082427

Goossens, S., Lemoine, F. G., Sabaka, T. J., Nicholas, J. B., Mazarico, E., Rowlands, D. D., Loomis, B. D., Chinn, D. S., Neumann, G. A., Smith, D. E.Zuber, M. T. (2016). A global degree and order 1200 model of the lunar gravity field using GRAIL mission data. In *47th Annual Lunar and Planetary Science Conference* (p. 1484). The Woodlands, Texas, USA. https://ui.adsabs.harvard.edu/abs/2016LPI....47.1484G

Hansen, P. C. (2000). The l-curve and its use in the numerical treatment of inverse problems. In P. Johnston (Ed.), *Computational Inverse Problems in Electrocardiology* (pp.119–142). Southampton: WIT Press

Hemingway, D., and Garrick-Bethell, I. (2012). Magnetic field direction and lunar swirl morphology: insights from Airy and Reiner Gamma. *J. Geophys. Res.: Planets*, *117*(E10), E10012. https://doi.org/10.1029/2012JE004165

Hemingway, D. J., and Tikoo, S. M. (2018). Lunar swirl morphology constrains the geometry, magnetization, and origins of lunar magnetic anomalies. *J. Geophys. Res.: Planets*, *123*(8), 2223–2241. https://doi.org/10.1029/2018JE005604

Hiesinger, H., Jaumann, R., Neukum, G., and Head, J. W. (2000). Ages of mare basalts on the lunar nearside. *J. Geophys. Res.: Planets*, *105*(E12), 29239–29275. https://doi.org/10.1029/2000JE001244

Hiesinger, H., Head, J. W., Wolf, U., Jaumann, R., and Neukum, G. (2003). Ages and stratigraphy of mare basalts in Oceanus Procellarum, Mare Nubium, Mare Cognitum, and Mare Insularum. *J. Geophys. Res.: Planets*, *108*(E7), 5065. https://doi.org/10.1029/2002JE001985

Holland, P. W., and Welsch, R. E. (1977). Robust regression using iteratively reweighted least-squares. *Commun. Stat. Theory Methods*, *6*(9), 813–827. https://doi.org/10.1080/03610927708827533

Hood, L. L. (2011). Central magnetic anomalies of Nectarian-aged lunar impact basins: probable evidence for an early core dynamo. *Icarus*, *211*(2), 1109–1128. https://doi.org/10.1016/j.icarus.2010.08.012

Hood, L. L., and Spudis, P. D. (2016). Magnetic anomalies in the Imbrium and Schrödinger impact basins: orbital evidence for persistence of the lunar core dynamo into the Imbrian epoch. *J. Geophys. Res.: Planets*, *121*(11), 2268–2281. https://doi.org/10.1002/2016JE005166

Hood, L. L., Torres, C. B., Oliveira, J. S., Wieczorek, M. A., and Stewart, S. T. (2021). A new large-scale map of the lunar crustal magnetic field and its interpretation. *J. Geophys. Res.: Planets*, *126*(2), e2020JE006667. https://doi.org/10.1029/2020JE006667

Jiang, C. Z., and Yao, S. (2019). 1D geothermal inversion of the lunar deep interior temperature and heat production in the equatorial area. *Phys. Earth Planet. Inter.*, *289*, 106–114. https://doi.org/10.1016/j.pepi.2019.02.007

Kurata, M., Tsunakawa, H., Saito, Y., Shibuya, H., Matsushima, M., and Shimizu, H. (2005). Mini-magnetosphere over the Reiner Gamma magnetic anomaly region on the moon. *Geophys. Res. Lett.*, *32*(24), L24205. https://doi.org/10.1029/2005GL024097

Lane, R. (2009). Some issues and insights for gravity and magnetic modelling at the region to continent scale. *ASEG Ext. Abstr.*, *2009*(1), 1–11. https://doi.org/10.1071/ASEG2009ab128

Li, Y. G., and Oldenburg, D. W. (1996). 3-D inversion of magnetic data. *Geophysics*, *61*(2), 394–408. https://doi.org/10.1190/1.1443968

Li, Y. G., and Oldenburg, D. W. (2003). Fast inversion of large-scale magnetic data using wavelet transforms and a logarithmic barrier method. *Geophys. J. Int.*, *152*(2), 251–265. https://doi.org/10.1046/j.1365-246X.2003.01766.x

Li, Y. G., Shearer, S. E., Haney, M. M., and Dannemiller, N. (2010). Comprehensive approaches to 3D inversion of magnetic data affected by remanent magnetization. *Geophysics*, *75*(1), L1–L11. https://doi.org/10.1190/1.3294766

Miljković, K., Wieczorek, M. A., Collins, G. S., Solomon, S. C., Smith, D. E., and Zuber, M. T. (2015). Excavation of the lunar mantle by basin-forming impact events on the moon. *Earth Planet. Sci. Lett.*, *409*, 243–251. https://doi.org/10.1016/j.epsl.2014.10.041

Nabighian, M. N. (1972). The analytic signal of two-dimensional magnetic bodies with polygonal cross-section: its properties and use for automated anomaly interpretation. *Geophysics*, *37*(3), 507–517. https://doi.org/10.1190/1.1440276

Oldenburg, D. W., and Li, Y. G. (1994). Subspace linear inverse method. *Inverse Probl.*, *10*(4), 915–935. https://doi.org/10.1088/0266-5611/10/4/011

Oliveira, J. S., and Wieczorek, M. A. (2017). Testing the axial dipole hypothesis for the moon by modeling the direction of crustal magnetization. *J. Geophys. Res.: Planets*, *122*(2), 383–399. https://doi.org/10.1002/2016JE005199

Purucker, M. E., and Nicholas, J. B. (2010). Global spherical harmonic models of the internal magnetic field of the Moon based on sequential and coestimation approaches. *J. Geophys. Res.: Planets*, *115*(E12), E12007. https://doi.org/10.1029/2010JE003650

Richmond, N. C., and Hood, L. L. (2008). A preliminary global map of the vector lunar crustal magnetic field based on Lunar Prospector magnetometer data. *J. Geophys. Res.: Planets*, *113*(E2), E02010. https://doi.org/10.1029/2007JE002933

Rochette, P., Gattacceca, J., Ivanov, A. V., Nazarov, M. A., and Bezaeva, N. S. (2010). Magnetic properties of lunar materials: meteorites, Luna and Apollo returned samples. *Earth Planet. Sci. Lett.*, *292*(3-4), 383–391. https://doi.org/10.1016/j.epsl.2010.02.007

Sonett, C. P., and Mihalov, J. D. (1972). Lunar fossil magnetism and perturbations of the solar wind. *J. Geophys. Res.*, *77*(4), 588–603. https://doi.org/10.1029/JA077i004p00588

Takahashi, F., Tsunakawa, H., Shimizu, H., Shibuya, H., and Matsushima, M. (2014). Reorientation of the early lunar pole. *Nat. Geosci.*, *7*(6), 409–412. https://doi.org/10.1038/ngeo2150

Tikoo, S. M., Weiss, B. P., Shuster, D. L., Suavet, C., Wang, H. P., and Grove, T. L. (2017). A two-billion-year history for the lunar dynamo. *Sci. Adv.*, *3*(8), e1700207. https://doi.org/10.1126/sciadv.1700207

Tsunakawa, H., Takahashi, F., Shimizu, H., Shibuya, H., and Matsushima, M. (2014). Regional mapping of the lunar magnetic anomalies at the surface: method and its application to strong and weak magnetic anomaly regions. *Icarus*, *228*, 35–53. https://doi.org/10.1016/j.icarus.2013.09.026

Tsunakawa, H., Takahashi, F., Shimizu, H., Shibuya, H., and Matsushima, M. (2015). Surface vector mapping of magnetic anomalies over the moon using Kaguya and Lunar Prospector observations. *J. Geophys. Res.: Planets*, *120*(6), 1160–1185. https://doi.org/10.1002/2014JE004785

Weber, R. C., Lin, P. Y., Garnero, E. J., Williams, Q., and Lognonné, P. (2011). Seismic detection of the lunar core. *Science*, *331*(6015), 309–312. https://doi.org/10.1126/science.1199375

Weiss, B. P., and Tikoo, S. M. (2014). The lunar dynamo. *Science*, *346*(6214), 1246753. https://doi.org/10.1126/science.1246753

Wieczorek, M. A., Weiss, B. P., and Stewart, S. T. (2012). An impactor origin for lunar magnetic anomalies. *Science*, *335*(6073), 1212–1215. https://doi.org/10.1126/science.1214773

Wieczorek, M. A., Neumann, G. A., Nimmo, F., Kiefer, W. S., Taylor, G. J., Melosh, H. J., Phillips, R. J., Solomon, S. C., Andrews-Hanna, J. C., … Zuber, M. T. (2013). The crust of the moon as seen by GRAIL. *Science*, *339*(6120), 671–675. https://doi.org/10.1126/science.1231530

Wieczorek, M. A. (2018). Strength, depth, and geometry of magnetic sources in the crust of the moon from localized power spectrum analysis. *J. Geophys. Res.: Planets*, *123*(1), 291–316. https://doi.org/10.1002/2017JE005418

Wilson, L., and Head, J. W. (2017). Generation, ascent and eruption of magma on the moon: new insights into source depths, magma supply, intrusions and effusive/explosive eruptions (part 1: theory). *Icarus*, *283*, 146–175. https://doi.org/10.1016/j.icarus.2015.12.039

Zuber, M. T., Smith, D. E., Lehman, D. H., Hoffman, T. L., Asmar, S. W., and Watkins, M. M. (2013). Gravity recovery and interior laboratory (GRAIL): mapping the lunar interior from crust to core. *Space Sci. Rev.*, *178*(1), 3–24. https://doi.org/10.1007/s11214-012-9952-7

Supplementary Materials for "Magnetized magma intrusions being sources of a weak and a strong lunar magnetic anomaly revealed by 3D distribution of magnetization"

Appendix A

A1. Depth Weighting Function

According to the analysis for a one-dimensional (1D) problem that $d_i = \int g_i(z)\, mz\mathrm{d}z$ where i = 0, 1, ... N, it is known that $g_i(z) = \mathrm{e}^{-az}\cos(2\pi iz)$ (Li YG and Oldenburg, 1996).

The decay factor e^{-az} is very important to determine the true depth of the magnetized body. For a cubic body, the numerical experiments indicate that $(z+z_0)^{-3/2}$ closely approximates the decay directly under the observation points, given a correctly chosen value of z_0. The comparison between $(z+z_0)^{-3/2}$ and e^{-az} is shown in Fig. 5 of Li YG and Oldenburg (1996). Therefore, the depth weighting function

$$w(z) = \frac{1}{(z+z_0)^{3/2}}$$

is set as part of the model objective function to obtain the correct burial depth of the magnetic carriers. An example is provided at https://giftoolscookbook.readthedocs.io/en/latest/content/fundamentals/WeightingMatrix.html.

We would like to clarify that the fraction function of depth z to approximate the decay factor is related to the shape of the magnetic source. In this work, the magnetic source is assumed to be sphere shaped, and the magnetic field decays by the inverse distance cubed (Cella and Fedi, 2012). Thus, the decay factor is set to be $(z + z_0)^{-3/2}$. For different shapes, the decay factor could be $(z + z_0)^{-k/2}$ with k = 0, 1, or 2 (Cella and Fedi, 2012). Because of insufficient information on the geological structure on the Moon, we do not know the true shape of the magnetic source. As a result, the magnetic carriers reconstructed by our work always show a sphere shape.

A2. Objective Function

The objective function $\phi(m)$ of the inverse problem is composed of two parts. One is the data misfit ϕ_d, and the other is the model objective function ϕ_m:

$$\begin{gathered}\phi(m) = \phi_d(m) + \beta\phi_m(m), \\ 0 < m < m_{\max}.\end{gathered} \tag{A1}$$

In Equation (A1), β is the regularization parameter and $m_{\max}$ = 400 A/m. This equation controls the relative importance of the model smoothness through the model objective function and the data misfit. When the standard deviations of data errors are known, an acceptable misfit is given. The β value could be looked for via the L-curve criterion or generalized cross-validation (Hansen, 2000; Farquharson and Oldenburg, 2004). How β affects the misfit and the recovered model of the inversion has already been checked. Examples are provided at https://giftoolscookbook.readthedocs.io/en/latest/content/fundamentals/Beta.html. The inverse problem is solved by finding a model m of magnetization that minimizes ϕ_m, misfits the data by a predetermined amount, and has magnetization within a sensible range.

The data misfit is defined by an L2 norm between the measured data $\boldsymbol{d}_{\mathrm{obs}}$ and the forward-calculated data from the underground magnetization model $\boldsymbol{d} = \boldsymbol{Gm}$:

$$\phi_d = \left|\boldsymbol{W}_d(\boldsymbol{Gm} - \boldsymbol{d}_{\mathrm{obs}})\right|_2^2. \tag{A2}$$

In Equation (A2), $\boldsymbol{W}_d$ is a diagonal matrix, whose ith diagonal component is $1/\sigma i$, and σi is the standard deviation of the ith datum. Data $\boldsymbol{d}_{\mathrm{obs}}$ denote the array of measured magnetic anomaly amplitudes at sites in a line on the surface. Thus, ϕ_d is a chi-squared variable distributed with N degrees of freedom. It should be noted that the contaminating noise in the data is independent and is Gaussian, with zero as the mean value. Normally, the target misfit is equal to N.

The model objective function ϕ_m is defined as follows:

$$\begin{aligned}\phi_m(m) =& \alpha_s\int_V w_s w(z)[m(r)-m_0]^2\mathrm{d}v + \\ & \alpha_x\int_V w_x\frac{\partial w(z)[m(r)-m_0]^2}{\partial x}\mathrm{d}v + \\ & \alpha_y\int_V w_y\frac{\partial w(z)[m(r)-m_0]^2}{\partial y}\mathrm{d}v + \\ & \alpha_z\int_V w_z\frac{\partial w(z)[m(r)-m_0]^2}{\partial z}\mathrm{d}v.\end{aligned} \tag{A3}$$

In Equation (A3), m is the model of magnetization, and $m_0 = 10^{-4}$ A/m is the initial reference model. The w_s, w_x, w_y, and w_z are spatially dependent weighting functions: w_s controls the similarity between the recovered model and the reference model, whereas w_x, w_y, and w_z control the gradient of magnetization, in case there is a geological structure. A larger w_x leads to a steeper gradient of magnetization along the x direction. If researchers do not know any special geological information about the region studied, the software used normally sets $w_s = w_x = w_y = w_z = 1$. Detailed information on the weighting matrices is provided at https://giftoolscookbook.readthedocs.io/en/latest/content/fundamentals/WeightingMatrix.html.

Variable $w(z)$ is the depth weighting function introduced in the first subsection of the Appendix, and α_s, α_x, α_y, and α_z are coefficients affecting the smoothness of the recovered model. Coefficient α_s controls the overall smoothness; a smaller α_s generates a smoother solution. Coefficients α_x, α_y, and α_z control the smoothness along the x, y, and z directions, respectively. If we do not have any geological information about the studied region, the aforementioned parameters are normally set as $\alpha_s = 10^{-4}$, and $\alpha_x = \alpha_y = \alpha_z = 1$. This means that the recovered distribution of magnetization is smoothly isotropic. How the α coefficients affect the inverse solution has been checked (see https://giftoolscookbook.readthedocs.io/en/latest/content/fundamentals/AlphaS.html).

Further, the model objective function can be expressed by the L2 norm or a sparse norm (L0-like norm). Its L2 norm expression is

$$\begin{aligned}\phi_m(m) &= (m-m_0)^{\mathrm{T}}(\alpha_s\boldsymbol{W}_s^{\mathrm{T}}\boldsymbol{W}_s + \alpha_x\boldsymbol{W}_x^{\mathrm{T}}\boldsymbol{W}_x + \alpha_y\boldsymbol{W}_y^{\mathrm{T}}\boldsymbol{W}_y + \alpha_z\boldsymbol{W}_z^{\mathrm{T}}\boldsymbol{W}_z)(m-m_0 \\ &= (m-m_0)^{\mathrm{T}}\boldsymbol{W}_{\boldsymbol{m}}^{\mathrm{T}}\boldsymbol{W}_{\boldsymbol{m}}(m-m_0) = |\boldsymbol{W}_{\boldsymbol{m}}(m-m_0)|^2,\end{aligned} \tag{A4}$$

The sparse norm (L0-like, or named L1 in mathematics) expression is

$$\phi_m(m) = \sum_{j=1}^{M} \ln\left(m_j^2\right). \tag{A5}$$

Because the sparse norm shows a more compact solution in the aspect of mathematics, the objective function is expressed in the sparse norm form.

The iteratively reweighted least squares (IRLS) algorithm is used to transform the sparse norm to a sequence of L2 norm inverse problems (Holland and Welsch, 1977):

$$\phi_m = |\boldsymbol{R}m|^2. \tag{A6}$$

In this expression, $\boldsymbol{R}$ is a diagonal matrix in which

$$r_{jj} = \left(\frac{\partial\phi_m\left(m^{n-1}\right)}{\partial_{m_j}^{n-1}}/m_j^{n-1}\right)^{1/2} = \left|m_j^{n-1}+\epsilon\right|^{-1}. \tag{A7}$$

The ε is a small constant to avoid the infinite r_{jj} when m_j equals 0.

A3. Solution to the Objective Function

To solve the model objective function, the logarithm barrier method is adopted (Li YG and Oldenburg, 2003). To the objective function is added a barrier item ϕ_λ as

$$\begin{aligned} \phi(\lambda) &= \phi_d(m) + \beta\phi_m(m) + \lambda\phi_\lambda(m) \\ \phi_\lambda &= -\sum_{j=1}^{M}\left[\ln\frac{m_j - m_{\min}}{m_{\max}-m_{\min}} + \ln\frac{m_{\max}-m_j}{m_{\max}-m_{\min}}\right]. \end{aligned} \tag{A8}$$

Next, one step of the Gauss–Newton method is applied. At the kth iteration, the following is obtained:

$$\begin{aligned} &(J^{(k)})^{\mathrm{T}}\boldsymbol{W}_d^{\mathrm{T}}\boldsymbol{W}_d J^{(k)} + \beta Z^{\mathrm{T}}\boldsymbol{R}^{\mathrm{T}}\boldsymbol{R}Z + \lambda^{(k-1)}[(X^{(k)})^{-2} + (Y^{(k)})^{-2}]\delta\boldsymbol{m} = \\ &\left(J^{(k)}\right)^{\mathrm{T}}\boldsymbol{W}_d^{\mathrm{T}}\boldsymbol{W}_d\left[\boldsymbol{d} - \boldsymbol{G}\boldsymbol{m}^{(k-1)}\right] - \beta Z^{\mathrm{T}}\boldsymbol{R}^{\mathrm{T}}\boldsymbol{R}Z\boldsymbol{m}^{(k-1)} + \lambda^{(k-1)}\left[\left(X^{(k)}\right)^{-1} + \left(Y^{(k)}\right)^{-1}\right]\boldsymbol{I}. \end{aligned} \tag{A9}$$

In Equation (A9), column vector $\boldsymbol{I}$ = [1, 1, 1, …]. For k = 1, the initial model $m^{(0)}$ equals the reference model m_0, where both are 10^{-4} A/m. The barrier item has $\lambda^{(0)} = \phi(m^{(0)})/\phi\lambda(m^{(0)})$. The $X^{(k)}$ and $Y^{(k)}$ are diagonal matrices having $m^{(k-1)} - m_{\min}$ and $m^{(k-1)} - m_{\max}$ on their main diagonals, respectively. Next, δm can be solved and $m^{(k)} = m^{(k-1)} + \lambda\beta^{(k)}\delta m$, in which γ = 0.925:

$$\beta^{(k)} = \begin{cases} 1, & \delta m > 0 \\ \min\dfrac{m_j^{(n-1)}}{\delta m_j}, & \text{others.} \end{cases} \tag{A10}$$

As a result, $\lambda^{(k)} = [1 - \min(\beta^{(k)}, \gamma)]\ \lambda^{(k-1)}$. Finally, it terminates on convergence or when k attains a maximum number for iteration. Otherwise, $k = k + 1$ goes to the loop again. In addition, the termination criterion is that the objective function changes less than 1% from the (k − 1)th to the kth iteration (Li YG and Oldenburg, 2003).

A4. Validity Check for the Lunar Condition

On Earth, the magnetization is usually assumed to be along the geomagnetic field. However, the direction of the ancient lunar dynamo field is unclear. Considering that the magnetization direction of the lunar crust is complex, the Curie depth is not yet clear, and the grid resolution of magnetic data is larger than that on the Earth, it is necessary to check whether the amplitude inversion is able to recover a synthetic model of magnetic carriers. A magnetized ball model is designed. The ball has a magnetization M = 1 A/m and a radius R = 1000 m. The depth to the center of the ball is 1100 m. This means that the depth to the top of the ball is 100 m. The inclination and declination of the magnetization of the ball are I = −75° and D = 0°, respectively. We take the downward component of the magnetic anomaly caused by a ball as an example to explain the free spatial unit:

$$\begin{aligned} Z_a = &\frac{\mu_0 MV}{4\pi(x^2+y^2+R^2)^{5/2}}\times \\ &[(2R^2 - x^2 - y^2)\sin I - 3Rx\cos I\cos D - 3Ry\cos I\sin D]. \end{aligned} \tag{A11}$$

In Equation (A11), V denotes the volume of the magnetized ball ($\frac{4\pi}{3}r^3$), R denotes the burial depth of the center of the ball, and x and y denote the position of the center of the ball at the horizontal plane. According to Equation (A11), if the units of r, R, x, and y are the same, such as kilometers rather than meters, the recovered distributions of magnetization are the same as those shown in the following figures (Figures A1–A3).

We carry on the validity tests of amplitude inversion for this synthetic magnetized ball in two steps. First, we check how the inverted magnetization is affected by the depth constraints. In this work, the magnetization direction is set to be I = −90° and D = 0° for the amplitude inversion. It should be noted that this direction is not the true one. The algorithm of the amplitude inversion used in this work can calculate only the magnitude of magnetization. The direction of magnetization has to be unified and assumed before inversion. The direction of remanent magnetization on the moon is much more complex than that on Earth. For the two regions studied, the magnetization direction calculated from the three components of magnetic anomalies is shown in Figure A4.

The distributions of magnetization recovered underground that are related to different depth constraints are shown in Figure A1. The magnetized ball is marked by white circles. The dotted contours denote 20% of the maximum value of magnetization. The bottom depths of the inversion region underground are set as 1100, 2000, 3000, and 5000 m. To check the solidity of the inversion results, the forward-calculated surface anomalies according to the inversion results are also shown in Figure A1. The correlation coefficients between the forward-calculated surface anomaly and the lunar anomaly model used are 1.00, 1.00, 1.00, and 1.00 for the depth constraints of 1100, 2000, 3000, and 5000 m. It is obvious that the bottom depth of the inversion region does not affect the recovered distribution of magnetization. The depth range and shape of the ball model can be accurately recovered. The grid spacing for both the surface anomaly and the inversion region underground is 50 m.

Second, we check how the inverted magnetization is affected by the grid resolution of the surface magnetic anomaly. The grid resolution of the lunar surface magnetic anomaly is known to be much larger than that on the Earth. For the same magnetized ball, we set the grid resolution of the surface magnetic anomaly at 50, 100, and 500 m. The bottom depth of the inversion regions is set at 3000 m. The direction of magnetization is still set at I = −90°

and D = 0° for the amplitude inversion. The grid resolution of the inversion region underground is always 50 m. The recovered magnetization underground is shown in Figure A2. We could identify that even if the grid resolution of the surface anomaly were to increase to half the radius of the magnetized body, the magnetized ball could still be accurately reconstructed. The concentration of the inverted body related to the larger grid resolution is lower than that of the true model. In addition, the forward-calculated surface anomaly from the inverted results is shown in Figure A2. The correlation coefficients between the input surface anomaly model and the forward-calculated surface anomaly are all 1.00 for the three grid resolutions.

Finally, we check how the wrong inclination affects the recovered magnetization underground, even though this was proved long ago. The true inclination of the magnetized ball is −75°. We try the inclination angles for every 15°; some of them are shown in Figure A3. The inclination angles are 15°, −30°, and −60°. We can identify that the depth to the top and that to the center of the magnetized body are the least affected by the inaccurate magnetization direction. The depth to the bottom of the recovered magnetized body varies by approximately 30%.

A5. Estimation of the Depth and Volume of the Magnetic Carriers

We suggest a quantitative criterion to determine the boundary of the magnetized body. Compared with the true model, the contour at 20% of the maximum magnetization is chosen to define the boundary of the magnetic carriers. From Figures A1 and A2, we can identify that such a contour is quite close to the boundary of the ball model. The depth to the top of the magnetic carriers is nicely recovered, whereas the boundary identified by this criterion is a bit wider and deeper than the model ball.

The depths to the top and that to the bottom of the critical contour are shown in Table A1, related to different depth constraints. The depth to the maximum magnetization (Max) is also shown. When the depth constraint is deeper than the bottom of the ball, the maximum magnetization corresponds to the center of the ball, and the depth to the bottom of the contour is deeper than that of the ball by approximately 25%. Note that the magnetization is not convergent and that it shows the maximum value at the bottom of the inversion region when the depth constraint is shallower than the depth to the bottom of the ball, as shown in Figure A1 and Table A1. The depth to the center of the magnetic carriers identified from the inversion by our criteria is rather accurate, with an uncertainty of less than 20%. Considering that the volume of the ball is 4.19 × 10^9 m^3, the recovered magnetic carriers are smaller by 5% when the depth constraints of the inversion region are 3000 and 5000 m.

A6. Complex Magnetization Directions in the Regions Studied

The inclinations of magnetic anomalies in Mare Tranquillitatis and in Oceanus Procellarum are calculated from the surface magnetic anomaly model shown in Figure A4.

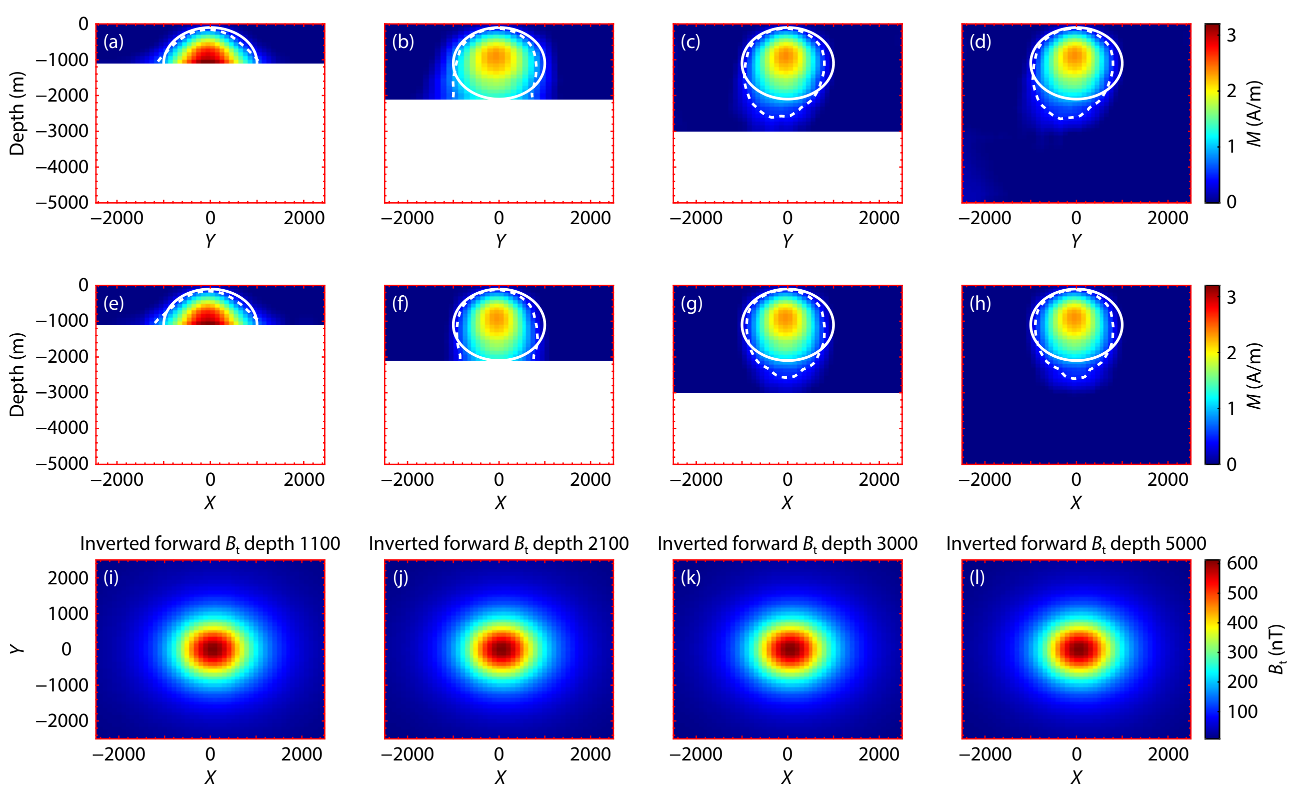

Figure A1. Magnetization underground recovered by amplitude inversion for a synthetic magnetized ball model with different depth constraints. From left to right, the depth constraints are 1100, 2100, 3000, and 5000 m. The distributions of magnetization in the depth–east profile at X = 50 are shown in the top row. The depth–north profiles at Y = 50 are shown in the second row. The white circles mark the ball model. The forward-calculated surface magnetic anomalies (B_t) from the inverted magnetization are shown in the bottom row. The dashed white contours mark 20% of the maximum magnetization.

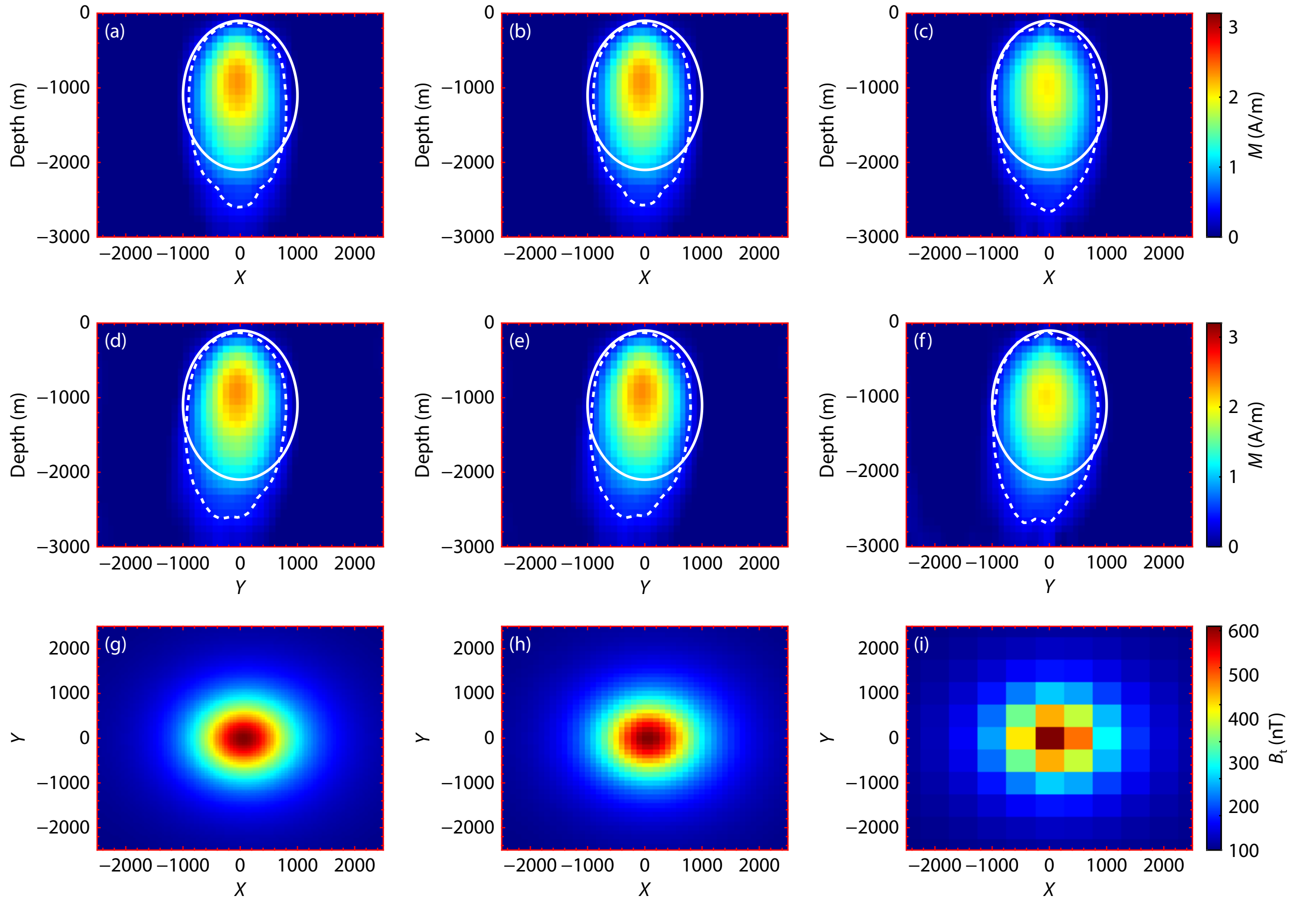

Figure A2. Magnetization underground recovered by amplitude inversion for a synthetic magnetized ball with different grid resolutions of a surface anomaly. From left to right, the grid resolutions of the surface anomaly are 50, 100, and 500 m. The distributions of magnetization in the depth–north profile at Y = 50 are shown in the top row. The depth–east profiles at X = 50 are shown in the second row. The forward-calculated surface anomalies from the inverted magnetization are shown in the bottom row. The white circles mark the ball model. The dashed white contours mark 20% of the maximum magnetization.

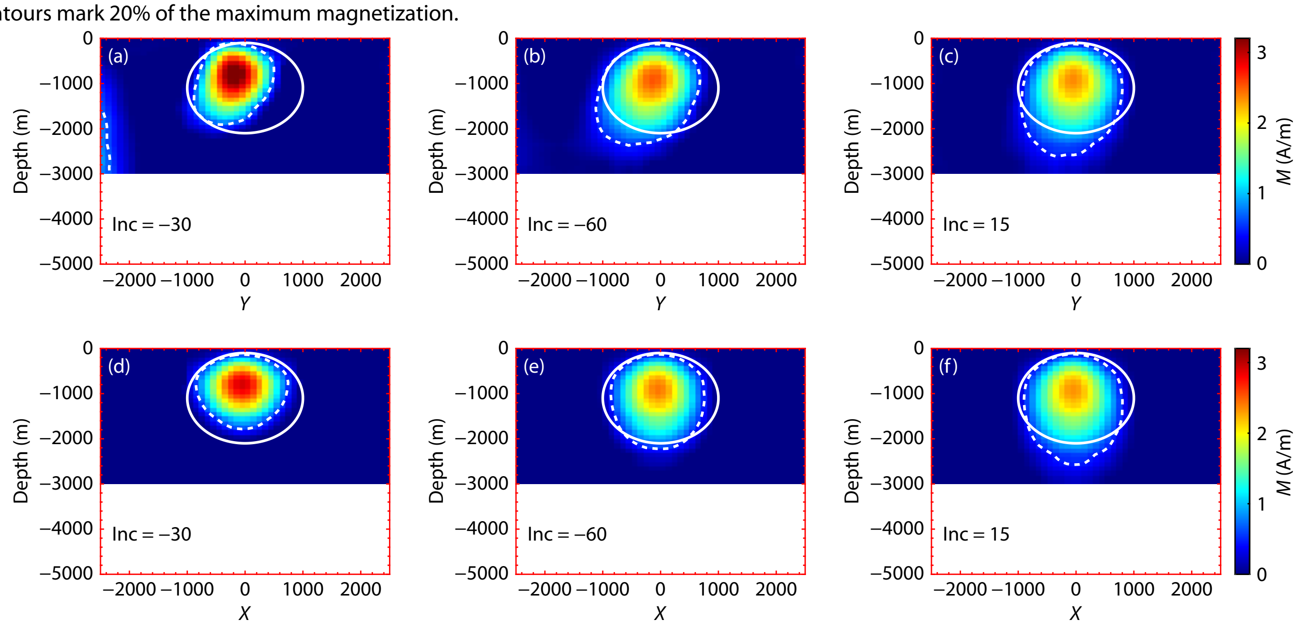

Figure A3. Magnetization underground recovered by amplitude inversion for a synthetic magnetized ball with different inclination angles. From left to right, the recovered magnetization is related to the inclination angles of −30°, −60°, and 15°. The top row shows the depth profiles along the Y direction at X = 50. The bottom row shows the depth profiles along the X direction at Y = 50. The solid white circles mark the ball model. The dashed white contours denote 20% of the maximum magnetization calculated by inversion.

Table A1. Depth ranges and volumes of the magnetized body recovered by inversion.

Depth constraint (km)	Profile	Top (m)	Max (m)	Bottom (m)	Volume (m^3)
TRUE	Latitude	−100.00	−1100.00	−2100.00	4.19×10^9
	Longitude	−100.00	−1100.00	−2100.00	
1100	Latitude	−158.64	−1100.00	−1050.00	1.69×10^9
	Longitude	−158.79	−1100.00	−1050.00	
2100	Latitude	−124.15	−1000.00	−2050.00	3.07×10^9
	Longitude	−124.12	−1000.00	−2050.00	
3000	Latitude	−126.33	−900.00	−2573.30	3.98×10^9
	Longitude	−125.72	−1000.00	−2613.20	
5000	Latitude	−125.72	−1000.00	−2607.40	3.96×10^9
	Longitude	−125.45	−900.00	−2653.30	

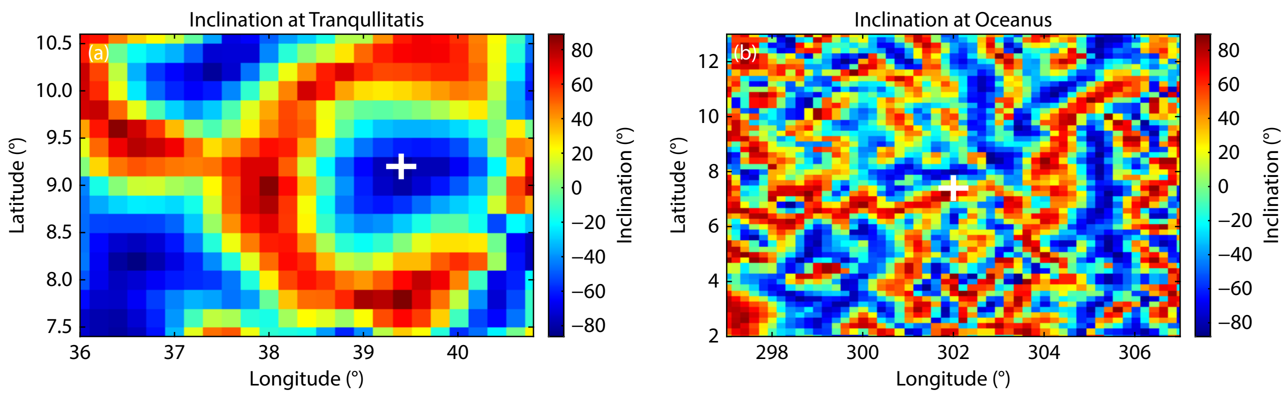

Figure A4. Distribution of the inclination calculated from the lunar surface magnetic anomaly model at Mare Tranquillitatis and Oceanus Procellarum. (a) The inclination of the anomaly at Mare Tranquillitatis. (b) The inclination of the anomaly at Oceanus Procellarum.